A SPITZER VIEW OF STAR FORMATION IN THE CYGNUS X NORTH COMPLEX

Accepted for publication in The Astrophysical Journal
Preprint typeset using LaTeX style emulateapj v. 11/10/09

A *SPITZER* VIEW OF STAR FORMATION IN THE CYGNUS X NORTH COMPLEX

I. M. Beerer,[1] X. P. Koenig,[2] J. L. Hora[2], R. A. Gutermuth,[34] S. Bontemps,[5] S. T. Megeath,[6], N. Schneider,[5] F. Motte[7], S. Carey,[8] R. Simon,[9] E. Keto,[2] H. A. Smith,[2] L. E. Allen,[8] G. G. Fazio,[2] K. E. Kraemer,[11] S. Price,[11], D. Mizuno,[12] J. D. Adams,[13] J. Hernández,[14] P. W. Lucas[15]

Accepted for publication in The Astrophysical Journal

ABSTRACT

We present new images and photometry of the massive star forming complex Cygnus X obtained with the Infrared Array Camera (IRAC) and the Multiband Imaging Photometer for *Spitzer* (MIPS) on board the *Spitzer Space Telescope*. A combination of IRAC, MIPS, UKIRT Deep Infrared Sky Survey (UKIDSS), and Two Micron All Sky Survey (2MASS) data are used to identify and classify young stellar objects. Of the 8,231 sources detected exhibiting infrared excess in Cygnus X North, 670 are classified as Class I and 7,249 are classified as Class II. Using spectra from the FAST spectrograph at the Fred L. Whipple Observatory and Hectospec on the MMT, we spectrally typed 536 sources in the Cygnus X complex to identify the massive stars. We find that YSOs tend to be grouped in the neighborhoods of massive B stars (spectral types B0 to B9). We present a minimal spanning tree analysis of clusters in two regions in Cygnus X North. The fraction of infrared excess sources that belong to clusters with $\geq$10 members is found to be 50–70%. Most Class II objects lie in dense clusters within blown out H II regions, while Class I sources tend to reside in more filamentary structures along the bright-rimmed clouds, indicating possible triggered star formation.

Subject headings: stars: formation — stars: pre-main sequence — infrared: stars — Stars: Early-Type—H II regions

1. INTRODUCTION

High-mass stars, though relatively rare, dominate the energetics of star formation in giant molecular clouds (Zinnecker & Yorke 2007). When high-mass stars form through the gravitational collapse of gas and dust, they release an immense amount of energy through stellar winds and radiation. The release of this energy has a profound effect on the massive star's environment, possibly inducing the formation of less massive stars in the surrounding area. Therefore, regions that contain massive stars provide excellent laboratories for studying both high and low mass star formation. By studying the distribution of young stellar objects (YSOs) in the neighborhood of massive stars, we hope to understand the relationship between high-mass stars, star formation and the interstellar medium (ISM).

Due to the high levels of extinction in star forming molecular clouds, the use of infrared imaging instruments on the *Spitzer Space Telescope* (Werner et al. 2004) has provided great insight into regions of star formation. *Spitzer* has been used to survey a number of star forming molecular clouds, e.g. W3 (Ruch et al. 2007), W5 (Koenig et al. 2008) and M17 (Povich et al. 2009; Povich & Whitney 2010). In these surveys, *Spitzer* was used to detect infrared excess emission from warm dust in disks and protostellar envelopes to map the spatial distribution of low and high mass YSOs within the molecular clouds. In this paper, we explore an active massive star-forming complex, Cygnus X, using photometry from the *Spitzer* Infrared Array Camera (IRAC) (Fazio et al. 2004) and the Multiband Imaging Photometer for *Spitzer* (MIPS) (Rieke et al. 2004).

Cygnus X is a $\sim 7^\circ \times 7^\circ$ region in the Cygnus constellation, which contains Gamma Cygni, the center star of the Northern Cross (Reipurth & Schneider 2008). First known for being a diffuse radio source, the region was named Cygnus X to distinguish it from the other radio source in Cygnus, the radio galaxy Cygnus-A (Piddington & Minnett 1952). Piddington and Minnett attributed the radio source to thermal emission from clouds of ionized gas. Extensive radio surveys of the region (Wendker 1984; Wendker et al. 1991, and references therein and subsequently) have confirmed that thermal emission dominates the radio wavelength output of Cygnus X, consistent with Cygnus X being the largest and most active region of star formation within 2 kpc of the Sun. It contains about 800 distinct H II regions, a number of Wolf-Rayet and OIII stars, several OB associations, and at least 40 massive protostars. Cygnus X also contains one of the most massive molecular cloud complexes in the nearby Galaxy, with a mass

[1] Department of Astronomy, University of California, Berkeley, CA, USA
[2] Harvard-Smithsonian Center for Astrophysics, 60 Garden St., Cambridge, MA, USA
[3] Smith College, Northampton, MA, USA
[4] Dept. of Astronomy, University of Massachusetts, Amherst, MA, USA
[5] Observatoire de Bordeaux, BP 89, 33270 Floirac, France
[6] Dept. of Physics and Astronomy, University of Toledo, Toledo, OH, USA
[7] AIM/SAp, CEA-Saclay, 91191 Gif Sur Yvette Cedex, France
[8] Spitzer Science Center, Pasadena, CA, USA
[9] I. Physik. Institut, Universität zu Köln, 50937 Köln, Germany
[10] NOAO, 950 North Cherry Avenue, Tucson, AZ, USA
[11] Air Force Research Laboratory, Hanscom AFB, MA, USA
[12] Institute for Scientific Research, Boston College, Boston, MA, USA
[13] Cornell University, Department of Radiophysics Space Research, Ithaca, NY, USA
[14] Centro de Investigaciones de Astronomía, Apdo. Postal 264, Mérida 5101-A, Venezuela
[15] Centre for Astrophysics Research, Science & Technology Research Institute, University of Hertfordshire, Hatfield, UK

of $\sim 3 \times 10^6 M_\odot$ (Schneider et al. 2006). Although once believed to be a superposition of many disconnected star formation regions, Schneider et al. (2006, 2007) showed that the molecular clouds in Cygnus X form connected groups at a distance of $\sim$ 1.7 kpc. The entire region exhibits evidence for many sites of star formation at different evolutionary stages, from the youngest embedded star formation in Infrared Dark Clouds (IRDCs) in DR21 (Downes & Rinehart 1966) to the young cluster Cygnus OB2 (Knödlseder 2000) to the more dispersed and perhaps older Cygnus OB9 region.

None of the nearby Galactic regions (within 2 kpc of the Sun) studied with *Spitzer* are as richly populated with massive stars as Cygnus X. Cygnus X is also near enough that the low-mass population can be detected in the same *Spitzer* observation. Observations indicate that around 75% of all stars form in clusters (Lada & Lada 2003; Carpenter 2000; Allen et al. 2007). Not all of the clusters in these studies have high mass stars however. Other molecular cloud surveys of massive star forming regions with *Spitzer* have revealed that 40–60% of the low-mass stars do not form in dense clusters (e.g. Koenig et al. 2008). The identification and classification of YSOs in Cygnus X enable us to study the spatial distribution of these objects around massive stars. Determining how many low mass stars form in clusters or in relative isolation will help us understand how low-mass stars form in molecular cloud complexes dominated by massive stars.

In this study, we used a combination of *Spitzer* infrared photometry and optical spectra from the Fast Spectrograph for the Tillinghast Telescope (FAST) and Hectospec on the MMT to make a census of the massive stars and the lower-mass YSOs in a $\sim 2^\circ \times 2^\circ$ region, termed Cygnus X North, centered roughly on the H II region, DR21.

We describe our observations in § 2. Our Cygnus X data were taken with the *Spitzer* IRAC and MIPS instruments as part of the Cygnus X Legacy Survey program (Hora et al. 2010). The optical spectra taken with the FAST and Hectospec instruments of stars in Cygnus X North are presented in § 2.4.

2. OBSERVATIONS AND METHODS

2.1. *IRAC Data*

Cygnus X was observed with the *Spitzer* IRAC instrument in all four bands (3.6, 4.5, 5.8, and 8.0 μm) in three campaigns between 2007 November and 2008 November. A *Spitzer* three-color composite image of Cygnus X North is shown in Figure 1. The RA and Declination for this and all subsequent figures is J2000.0. The IRAC pixel scale is 1.2″ pixel^{-1}. The Cygnus X region was mapped by raster-scanning across the field using offsets of 100″ in one direction and 300″ in the other, resulting in at least three frames at each integration time at each position on the sky. The observations were taken in HDR mode, in which a 10.4 s frame and a 0.4 s frame were obtained at each position. Basic Calibrated Data (BCD) version 18.7 images from the *Spitzer* Science Center's standard pipeline were used. These data were combined into mosaics using WCSmosaic (Gutermuth et al. 2008). The BCD images were improved by locating and removing the column pull-down and mux-bleed artifacts and the banding effects.

TABLE 1
Source Classification Summary

Class	Number of Objects
Class I	670
Class II	7,249
Embedded protostars	200
Transition Disks	112
Photospheres	350,058
Other [1]	677
Unclassified	311,192
Total	670,158

[1] Includes PAH emission dominated sources, H_2 shock emission dominated sources and broad-line AGN candidates. Unclassified sources lack detection in 4 bands (either HK_S, IRAC 1 and 2, or IRAC 1, 2, 3 and 4) or a bright MIPS 24 μm detection.

Automated source detection and aperture photometry were carried out on all point sources using PhotVis version 1.10 (Gutermuth et al. 2008). PhotVis, a photometry visualization tool, utilizes a DAOphot source-finding algorithm. The aperture photometry was performed with synthetic apertures of 2.4″ radius and background annuli of inner and outer radii of 2.4″ and 7.2″, respectively. The software filters outlier pixel values in the background annuli via iterative statistics and adds the measured standard deviation of the kept pixels in quadrature with the shot noise estimates for the final mean background flux per pixel and the shot noise in the main aperture. The photometry was calibrated with the following values (Vega-standard magnitudes for 1 DN s^{-1}): 19.455, 18.699, 16,498, and 16.892 for 3.6, 4.5, 5.8, and 8.0 μm bands, respectively. The completeness of the survey was estimated by adding artificial sources of various magnitudes and performing the photometry on the mosaics in the same way as was done to generate the real catalog. The IRAC point spread function was used to add the simulated sources into the images. In order for the source to be recovered, it had to be within an arcsec of the position it was inserted and within a half magnitude of the input value. Objects that fall close to bright stars or bright, structured nebulosity were not recovered. The 90% completeness levels for IRAC channels 1, 2, 3, and 4 are 14.98, 14.87, 13.82, and 12.60, respectively (Hora et al. 2010). Final photometric errors include the uncertainties in the zero-point magnitudes ($\sim$0.03 mag).

2.2. *MIPS Data*

The MIPS observations were taken at the fast scan rate, with a typical resolution of 6″ in the 24 μm band. Only the 24 μm data are considered here. The data were reduced and mosaicked using the MIPSGAL processing pipeline (Mizuno et al. 2008; Carey et al. 2009). Point source photometry was extracted using Cluster Grinder and PhotVis (Gutermuth et al. 2008). A synthetic aperture radius of 7.6″ and background annulus inner and outer radii of 7.6″ and 17.8″ was used. The photometry was calibrated with the value 14.6 mag for 1 DN s^{-1}.

2.3. *YSO Classification*

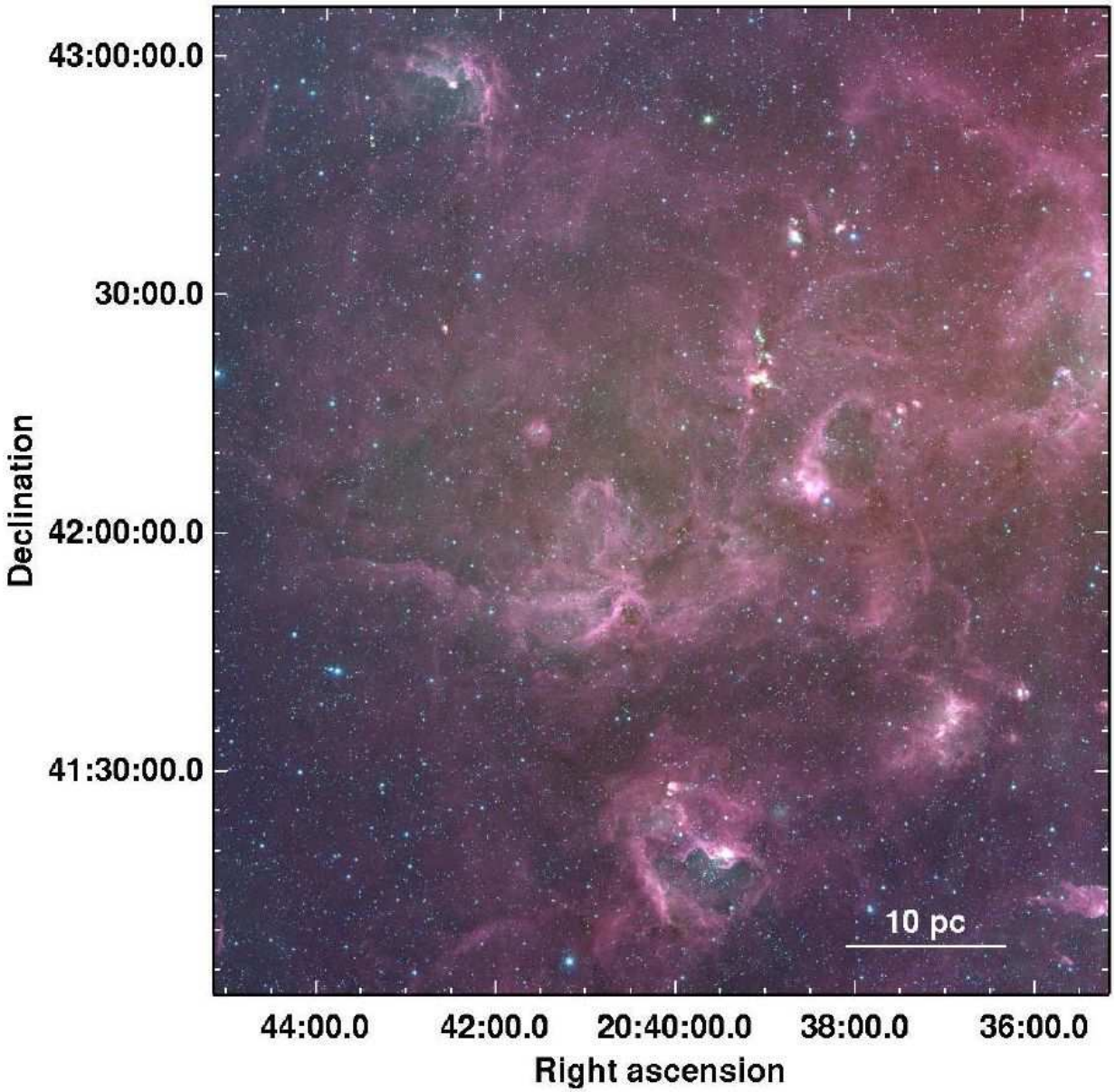

FIG. 1.— *Spitzer* IRAC three-color composite image of Cygnus X North. *red*: 8.0 μm; *green*: 4.5 μm; *blue*: 3.6 μm. The coordinate axes are in J2000.0 epoch.

Young stars emit excess radiation in the infrared compared with that seen in main-sequence stellar photospheres, due to thermal emission from the YSO's circumstellar material. Thus, YSOs can be identified by looking for infrared excess emission.

YSOs are categorized into Class 0, I, II or III evolutionary stages. Class 0 objects are deeply embedded protostars that are still experiencing cloud collapse. Since they are so embedded, they are extremely faint at wavelengths shorter than 10 μm. They have a significant submillimeter luminosity: $L_{\rm submm}/L_{\rm bol} > 0.5\%$. A Class I YSO is also an object whose emission is dominated by a dense infalling spherical envelope but is infrared bright. With only infrared data it is usually not possible to distinguish Class 0 from Class I objects. A Class II YSO is characterized by the presence of an optically thick, primordial circumstellar disk, which dominates the star's emission. When most of the circumstellar disk material has become optically thin, the star is classified as a Class III star. Thus, a Class III object is a pre-main sequence star that has lost its accretion disk, but may exhibit a small amount of infrared excess due to a secondary/debris disk. In this paper we additionally catalog a further class of YSO, the "transition disk" (TD). These objects display an intermediate infrared excess morphology between Class II and III as they exhibit disks, but with evidence for significant dust clearing in the inner disk region. They exhibit emission consistent with reddened photospheres that have IR excess at 24 μm and longer wavelengths. There is some debate in the literature as to their exact place in the evolutionary path from Class II to Class III however (e.g. Hernández et al. 2008; Currie et al. 2010).

The circumstellar material around a young star disap-

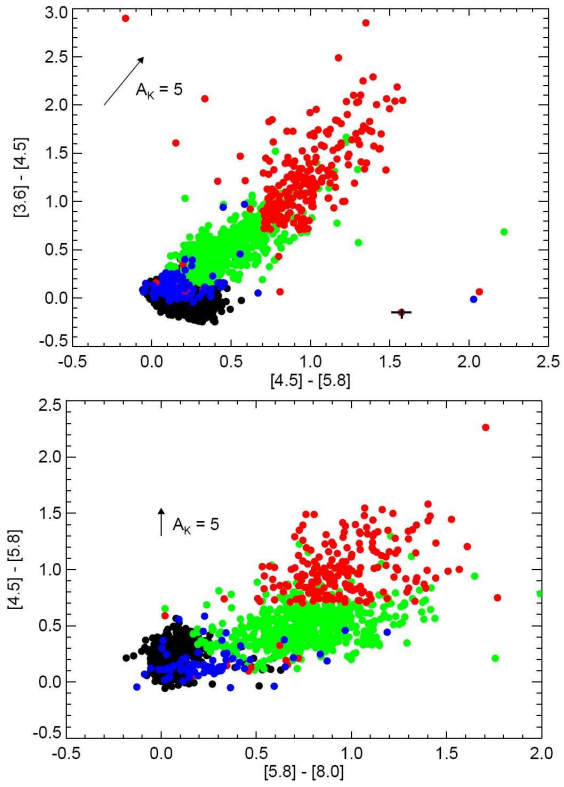

FIG. 2.— *Top*: [3.6]-[4.5] vs. [4.5]-[5.8]; *Bottom*: [4.5]-[5.8] vs. [5.8]-[8.0] IRAC color-color diagrams used for identifying YSOs. One red dot shows error bars in black. *Black dots*: Photospheres; *green*: Class II; *red*: Class I; *blue*: Transition Disk Candidates.

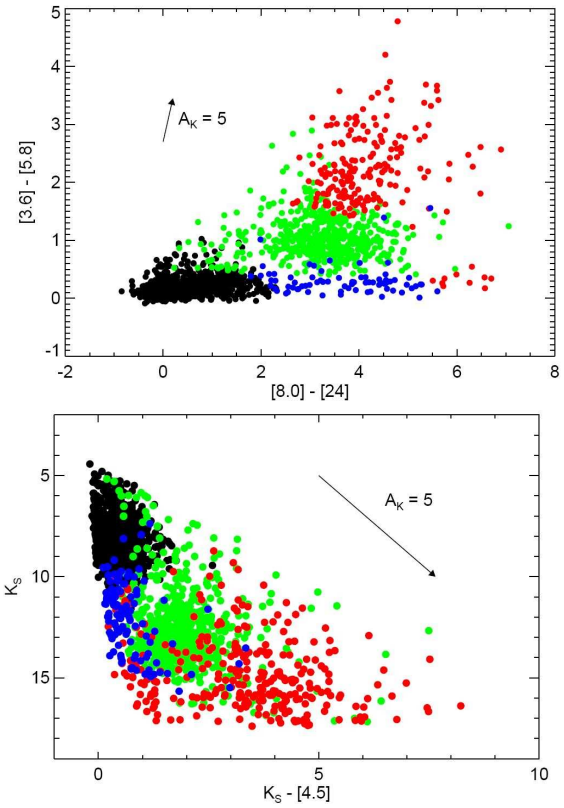

FIG. 3.— *Top*: [3.6]-[5.8] vs. [8.0]-[24] IRAC and MIPS color-color diagram; *Bottom*: 2MASS [K] vs. [K]-[4.5] color-magnitude diagram used for identifying YSOs. *Black dots*: Photospheres; *green*: Class II; *red*: Class I; *blue*: Transition Disk Candidates.

pears as the star evolves, and consequently the infrared excess emission decreases. Thus, by measuring the star's IR excess—once it has become visible in the infrared—we can determine its evolutionary state. Since younger stars are brighter at longer IR wavelengths, we can classify YSOs by calculating the slope of the source's spectral energy distribution (SED), which is defined as:

$$\alpha = \frac{d\log(\lambda F_\lambda)}{d\log(\lambda)} \quad (1)$$

where F_λ is the star's flux density at wavelength, λ.

Color-color and color-magnitude diagrams, which compare the ratio of a star's flux in different bands, can be used to look for IR excess to classify YSOs in place of calculating α for each object. We used IRAC, MIPS, Two-Micron All-Sky Survey (2MASS, Skrutskie et al. 2006) and UKIRT Deep Sky Survey DR4 (UKIDSS, Lawrence et al. 2007; Lucas et al. 2008) photometry to classify the YSOs in Cygnus X using the classification scheme presented in Gutermuth et al. (2008), with the extinction map of Schneider et al. (2006) generated from 2MASS data used to deredden the photometry. Figures 2 and 3 show example color-color and color-magnitude diagrams that were used to classify the YSOs. The points are plotted without dereddening their photometry. The scheme also provides a means of filtering out extragalactic sources (for example, active galactic nuclei or AGN) on the basis of magnitude and color cuts.

Using these methods, we found 670 Class I, 7,249 Class II and 350,058 normal photospheres in the Cygnus X North region. We also identified 200 deeply embedded objects (with SEDs resembling Class I sources but showing evidence for large optical extinction) and 112 transition disks. These classifications are summarized in Table 1.

In the left panel of Figure 2, one red Class I source shows error bars. We calculated the errors in color by adding the median uncertainty in magnitude for the two channels in quadrature. We also show the extinction vector in each plot for that filter combination using the extinction law derived by Flaherty et al. (2007). The typical line of sight extinction to sources in Cygnus X is $A_K = 0.5$ to 1.0 (Schneider et al. 2006). Thus, except for the most embedded sources, neither photometry error or reddening are responsible for the distribution of sources on these color-color diagrams and the dominant contributor to their colors is the intrinsic spread in properties of the sources. In Figure 4, we show the number of YSOs (including Class I, II, deeply embedded protostars and transition disks) detected in each of the four IRAC bands per magnitude, in comparison to all detected stellar sources. Firstly we note that channels 3 and 4 detect far fewer sources than channels 1 and 2. This deficit exists because channels 1 and 2 are more sensitive than channels 3 and 4 and are also less affected by the bright diffuse emission that dominates the channel 3 and 4 images. The underlying typical stellar photosphere is also intrinsically fainter at 5.8 and 8 μm than at 3.6 and 4.5 μm, which further hinders our ability to detect sources in the longer wavelength IRAC filters. Secondly, there is a flattening off in the YSO histograms at the brightest magnitudes in all bands. We

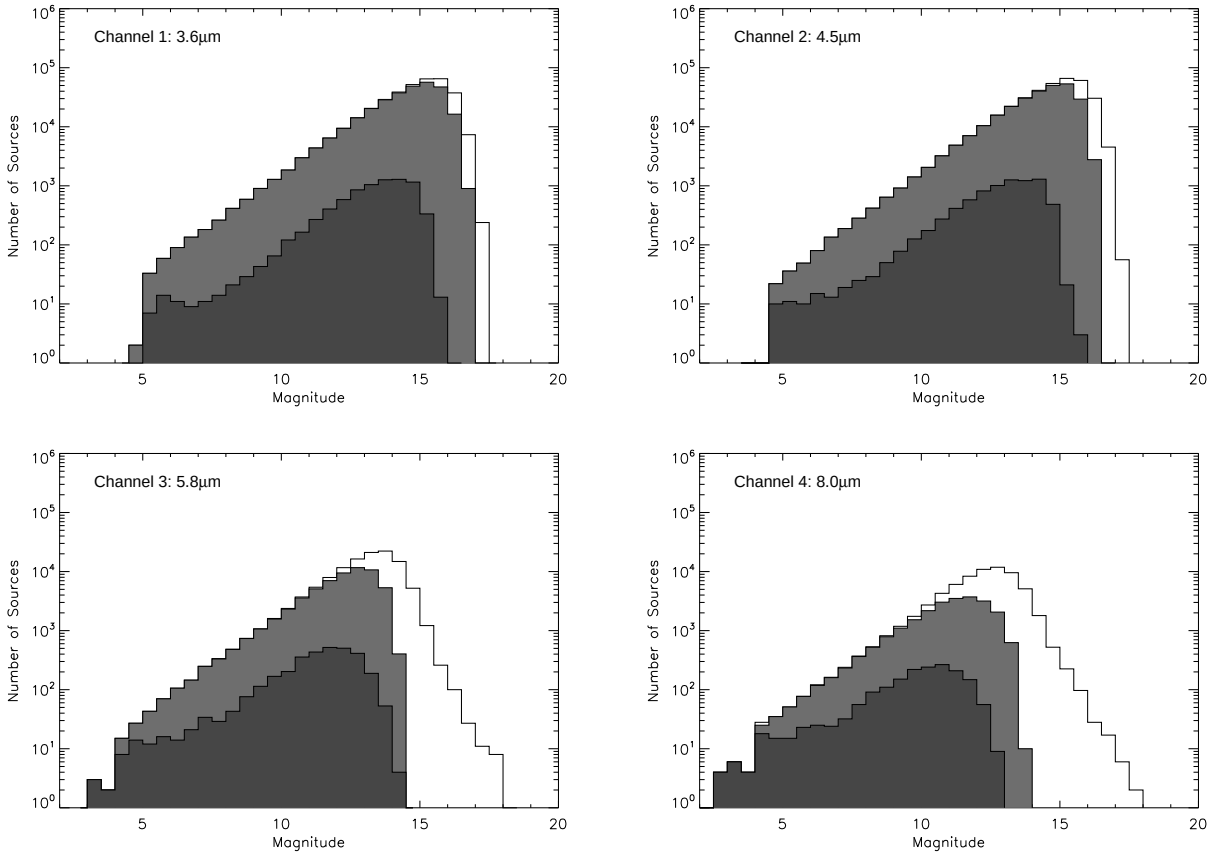

FIG. 4.— Apparent magnitude histograms of detections for all IRAC bands of all stellar sources (white histogram), stellar sources with error <0.1 mag (light gray histogram) and YSOs with error <0.1 mag (dark gray histogram) in Cygnus X North.

attribute this trend to contamination, likely from AGB stars. As found by Robitaille et al. (2008), a majority of objects brighter than $[4.5] = 7.8$ in a typical Galactic field are so-called "extreme" AGB stars, while sources fainter than this cut are either "Standard" AGB stars or YSOs. In Cygnus X this contamination reveals itself in the apparent increased proportion of YSOs amongst the overall stellar populations in each IRAC histogram at the brightest magnitudes (brighter than 8th magnitude in any band).

2.4. *Optical Spectroscopy*

To study the effect massive stars have on their environment in Cygnus X, we need to first identify the most massive stars. Then, we can investigate how the young stellar objects form in their presence. Using r' and i' magnitudes from the IPHAS survey (Drew et al. 2005), we identified a sample of possible O and B type stars in the $2^\circ \times 2^\circ$ field near DR21 in Cygnus X (González-Solares et al. 2008). We obtained 536 optical spectra during Fall 2008 using the FAST instrument, an optical spectrograph in operation at the focus of the 1.5 m Tillinghast reflector at the Fred L. Whipple Observatory on Mt. Hopkins (Fabricant et al. 1998) and the Hectospec multifiber spectrograph mounted on the 6.5 m MMT telescope on Mount Hopkins (Fabricant et al. 1994). The FAST spectra were obtained using the 300 groove mm^{-1} grating centered at 5500 Å with a resolution of 3 Å and processed using the standard FAST pipeline reduction (Tokarz & Roll 1997). Figure 5 presents example FAST spectra from our sample.

Hectospec is a multi-object spectrograph with 300 fibers that can be placed within a 1° diameter circular field. We used the 270 groove mm^{-1} grating, and obtained spectra in the range 3700–9000 Å with a resolution of 6.2 Å. Data reduction was performed by S. Tokarz through the CfA Telescope Data Center, using IRAF tasks and other customized reduction scripts. The reduction procedure was the standard for the Hectospec data, with the addition of our special sky subtraction procedure. To avoid the difficulties encountered when subtracting a sky spectrum made from an average over the highly variable H II region, we took exposures offset by $\sim 5''$ after each Hectospec configuration. This way we obtained a sky spectrum very close to each star through the same fiber. Background subtraction was performed in IDL to remove each wavelength calibrated sky offset spectrum from its corresponding wavelength calibrated object spectrum.

To classify our sources, we used the spectral classification code SPTclass[16] (Hernández et al. 2004; Hernández 2005). This automated code can classify spectra to a precision of half a subtype (e.g. G6.5±0.5). It uses only spectral line ratios, not continuum shape and is currently unable to distinguish the luminosity class of the star being classified. Of the 536 spectra, 24 sources were clas-

[16] http://www.astro.lsa.umich.edu/∼hernandj/SPTclass/sptclass.html.

TABLE 2
Spectral Classification Summary

Spectral Type	Number
B	24
A	49
F	229
G	146
K	81
M	7

sified as B type stars. The most massive star identified was a B0.0±2.0. The fact that we did not find any O type stars may be a result of our selection criteria. We selected sources from the IPHAS survey, which does not include any sources brighter than magnitude 10. Therefore, our survey may be missing some of the brightest sources. Figure 6 shows the optical color-magnitude distribution of IPHAS photometry for sources for which we obtained spectra. The region above the black dashed line is the expected location of O stars at the distance of Cygnus X (1.7 kpc). Although we have some spectra in this region, the sampling is sparse. We searched the literature for massive stars that were identified in previous studies. Comerón et al. (2008) found one object (star 100 in their catalog) classified as O9V in the vicinity of the Diamond Ring (DR 17). They also identify many candidate early-type stars in this region, although these lack a precise spectral type. Wendker et al. (1991) discuss the radio continuum emission at 408 and 4800 MHz in the environment of this portion of Cygnus X and show that it is made up of numerous thermally emitting H II regions, that are likely powered by massive O stars. We thus attribute our lack of confirmed spectroscopic O stars to a simple sampling effect. Table 2 summarizes our spectral classification results. The drop in number of objects classified later than spectral type F (G, K and M) is due to the spectral sample selection which preferentially chose the bright, blue targets and the sensitivity limits of our spectral survey. The full listing of sources for which we determined classifications, along with their positions, spectral types and uncertainties is presented in the Appendix.

3. ANALYSIS

3.1. *Color-Magnitude Diagram*

To verify that the sources for which we have optical spectra are indeed members of the Cygnus X complex, we plot the spectroscopic sample on a dereddened color-magnitude diagram. We used the catalog of spectral types and intrinsic colors presented in Kenyon and Hartmann (1995) to determine each star's intrinsic $r'-i'$ color via the Sloan filter conversions presented in Jordi et al. (2006). These colors allow us to calculate the visual extinction, A_V toward each object using the relation between A_λ and A_V given in Schlegel et al. (1998). The dereddened color-magnitude diagram of the 536 sources in Cygnus X for which we have optical spectra is shown in Figure 7 with isochrones from Siess et al. (2000) shifted to a distance of 1.7 kpc (red solid lines). We can see that in general the sources fall between the isochrones at 1 and 5 Myr, which we would expect given the large amount

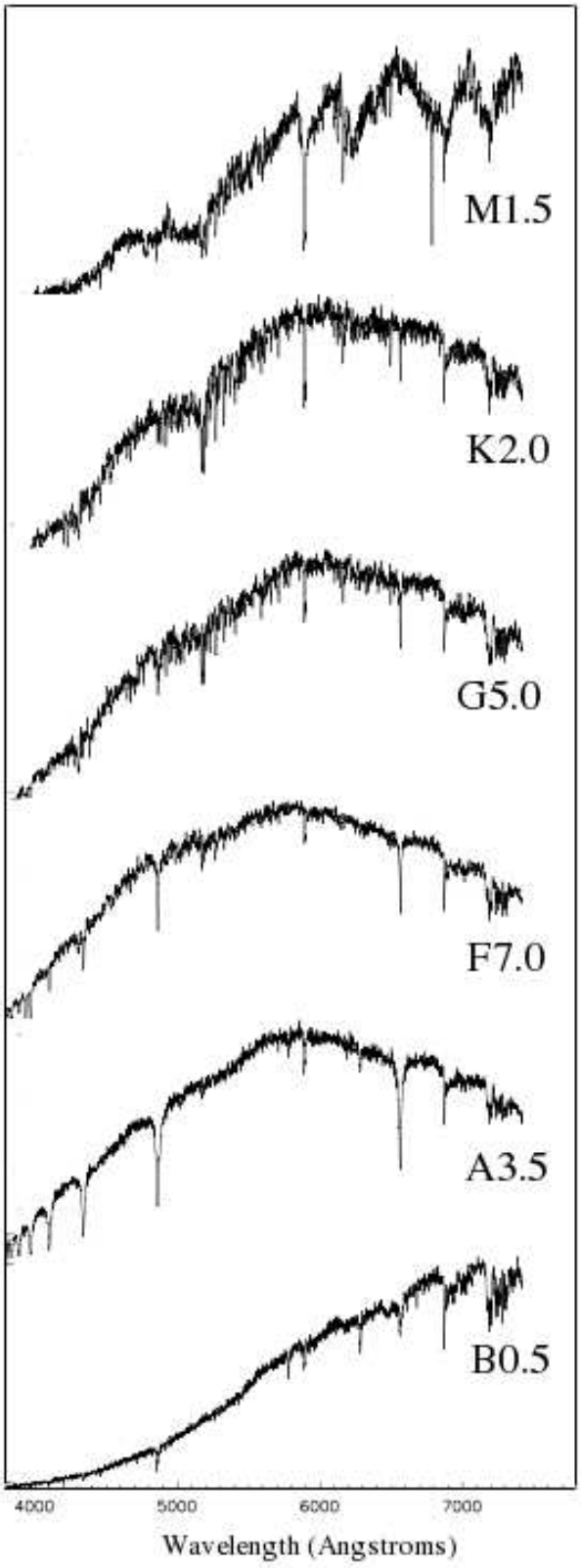

Fig. 5.— Examples of our FAST optical spectra for each spectral type.

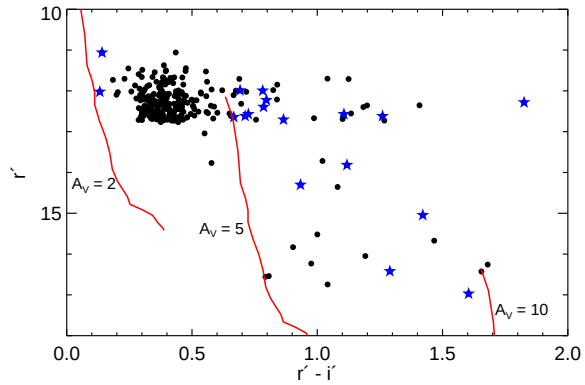

FIG. 6.— Color-magnitude diagram of the spectroscopic sample in this paper. Blue star symbols mark objects classified as B stars. Solid red lines show the main sequence between B0 and B9 at a distance of 1.7 kpc at A_V=2, 5 and 10 from Kenyon & Hartmann (1995). Black dashed line shows expected locus of B0V stars at a distance of 1.7 kpc over the same range of optical extinction.

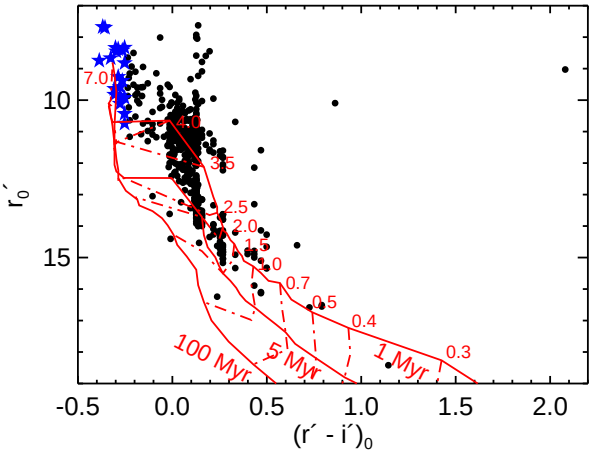

FIG. 7.— Dereddened optical color-magnitude diagram of all sources for which we have optical spectral classifications. B type stars are plotted with blue star symbols. A through M type stars are plotted in black. Red solid lines show isochrones for 1 Myr, 5 Myr, and 100 Myr from Siess et al. (2000). Red dash-dotted lines show corresponding mass tracks, masses are marked in $M_\odot$.

of embedded star formation in this part of Cygnus X. In particular, the location of the B stars (shown with blue stars in Fig. 7) is consistent with their being at the accepted distance of Cygnus X of 1.7 kpc and thus being members of the region. It is clear however that there are many later type sources which are above the 1 Myr isochrone, which could be very young stars or objects in the foreground.

3.2. *Spatial Distribution of YSOs in Cygnus X*

Figure 8 shows the spatial distribution of the YSOs overlaid on the IRAC 8.0 μm gray-scale image of the north-eastern part of Cygnus X. The sources are colored according to their evolutionary class. Although young stars are distributed throughout the field of view, the figure shows obvious regions of higher stellar densities. B stars are marked with orange asterisks. The image shows that the dense clumps of YSOs tend to be concentrated near the massive B stars. However, there are some B stars that appear distant from any clustering. Since Cygnus X lies along the Galactic Plane, our source list of YSOs is likely contaminated by some foreground and background young stellar populations. We estimate an upper limit to this contamination by measuring the source density in regions of the lowest density of YSOs in the complete Cygnus X survey (Hora et al. 2010) that lie along the Galactic Plane. This method will clearly produce an overestimate of the level of contamination as many of these sources will belong to Cygnus X. We find a density of 537 sources per square degree. We consider this level of contamination low enough to ignore for the purposes of this particular study.

Many Class I and II objects are clustered together within clouds of bright IR emission, while others form filamentary structures. For example, the DR22 region shows a dense cluster of Class II sources inside a large cavity where the gas appears to have been blown out, presumably due to the presence of a massive star. This cluster was also noted by Dutra & Bica (2001) and Le Duigou & Knödlseder (2002). In this region, we can see Class I objects residing in more filamentary structures along the rim of the cloud. One branch of Class I objects extends north in the direction of the DR23 region, along the DR22-DR23 molecular CO filament detected by Schneider et al. (2006). DR23 is another example of a dense concentration of Class II sources surrounded by a ring of Class I sources along a bright-rimmed cloud. Northwest of this structure is the H II region, DR21 (Downes & Rinehart 1966). The dense cluster of YSOs in DR21 form an extraordinarily straight chain.

Cygnus X provides a rich and varied collection of YSO clusters for our study of star formation. To understand the intricate substructure of the Cygnus X region, we selected two smaller areas in this field of view to study in more detail. The first region, shown in Figure 9, lies just slightly southwest of DR21 and is termed the Diamond Ring. We can see a bright ring of emission, around which lie many dense clusters of YSOs, in addition to six identified B stars. The second region, AFGL 2636, is in the northeast corner of Figure 8. Inside an arch of bright emission, there is a dense group of Class II objects and three B stars. A chain of Class I sources along the rim of the cloud extends in a long ring to another dense cluster to the east.

3.3. *Clustered Star Formation in Cygnus X*

To understand the evolution of star formation in Cygnus X, we would like to be able to identify distinct clusters of young stars and draw conclusions on their evolution based on comparisons of their relative sizes and ages. However, there are many obstacles to being able to glean such information. First, we have no insight on the gravitational relationships between the stars. Therefore, we must determine cluster memberships based on the spatial distribution of the sources. Although we assume all the sources are at about the same distance (1.7 kpc) due to their IR excess emission, we do not know the exact three-dimensional position of each star within the cloud. Second, stars do not form neatly in distinct, independent clusters. Clusters vary greatly in size, shape and density and can interact and overlap with other clusters, which renders defining cluster membership somewhat arbitrary. Therefore, to quantitatively describe the clusters in Cygnus X in such a way that we can compare with sim-

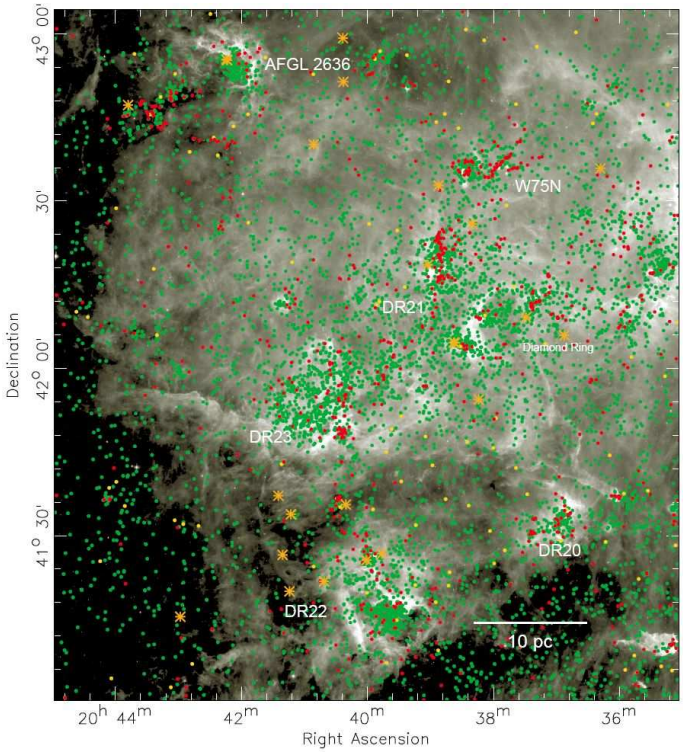

FIG. 8.— Distribution of YSOs overlaid on IRAC channel 4 (8.0 μm) gray-scale image. *Red*: Class 0 and I; *green*: Class II; *yellow*: Transition Disks. Orange asterisks indicate B stars. The coordinate axes are in J2000.0 epoch.

ilar studies of other star-forming regions, we chose to use the cluster isolation method described and extensively tested in Gutermuth et al. (2009). This method, which relies on the minimal spanning tree (MST) construction (Cartwright & Whitworth 2004), has been used recently by Koenig et al. (2008) to characterize clusters with IRAC and MIPS photometry in W5. Since our cluster isolation technique relies only on a measure of the local surface density of stars, it is a *relative* method. Given the lack of information on the dynamical properties and masses of the stars, an algorithm to isolate contiguous, locally overdense structures is the most appropriate tool that we can use in this case.

3.3.1. *The Diamond Ring*

Located southwest of DR21 lies the region dubbed the "Diamond Ring" by Marston (2004). The Diamond Ring, which is shown in Figure 9, is believed to have been formed by a H II region identified by a 3 cm radio survey by Lockman (1989). Marston et al. point out that the filaments extending from DR21, which can be seen in the top-left of Figure 9, are truncated by the Diamond Ring and therefore, conclude that this structure is at the same distance as DR21. The very bright tip of the Diamond Ring has been identified previously as the site of a stellar cluster using 2MASS J, H and K_S data (Object 16 and Cl 13 in Dutra & Bica (2001) and Le Duigou & Knödlseder (2002), respectively). Using the 2MASS photometry and assuming a distance modulus of 11^m, Le Duigou & Knödlseder (2002) inferred that this cluster contains 12 B stars and no O stars. We found two B stars in the bright tip of the diamond, a B0.5

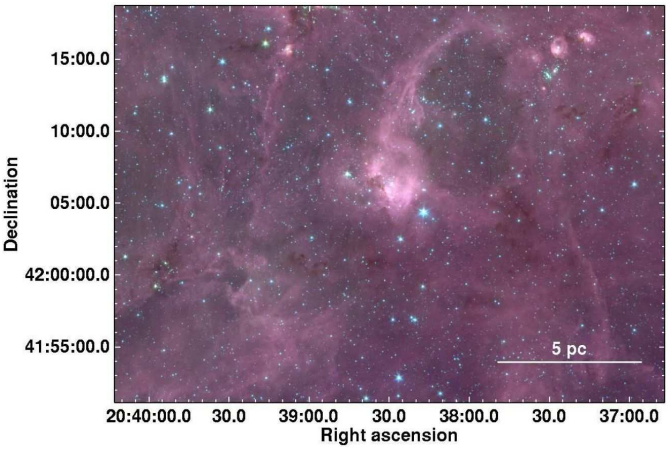

FIG. 9.— IRAC three-color composite image of the Diamond Ring. *red*: 8.0 μm; *green*: 4.5 μm; *blue*: 3.6 μm.

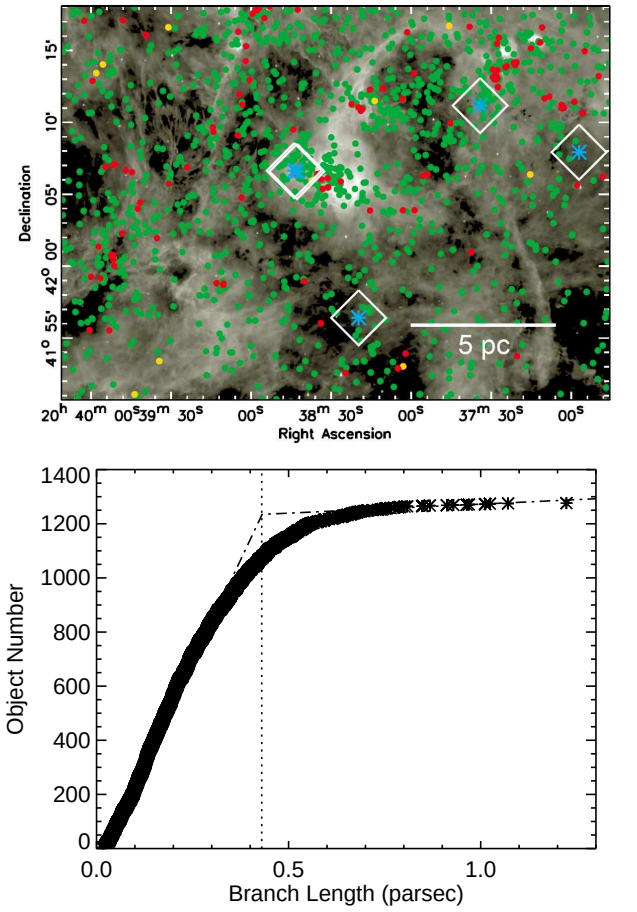

FIG. 10.— *Top*: YSO distribution overlaid on IRAC 8.0 μm gray-scale image of the Diamond Ring. *Red*: Class0/ I; *green*: Class II; *yellow*: Transition Disks. Blue asterisks and white boxes mark B stars. *Bottom*: MST branch length distribution. The objects are sorted in order of increasing branch length. We fit straight lines through the long and short branch length domains. The point of intersection, d_c = 0.43 pc, is chosen for the cutoff distance for cluster determination.

and a B9.0. We identified five B stars in the entire region, which are shown as blue asterisks in Figure 10 (left panel).

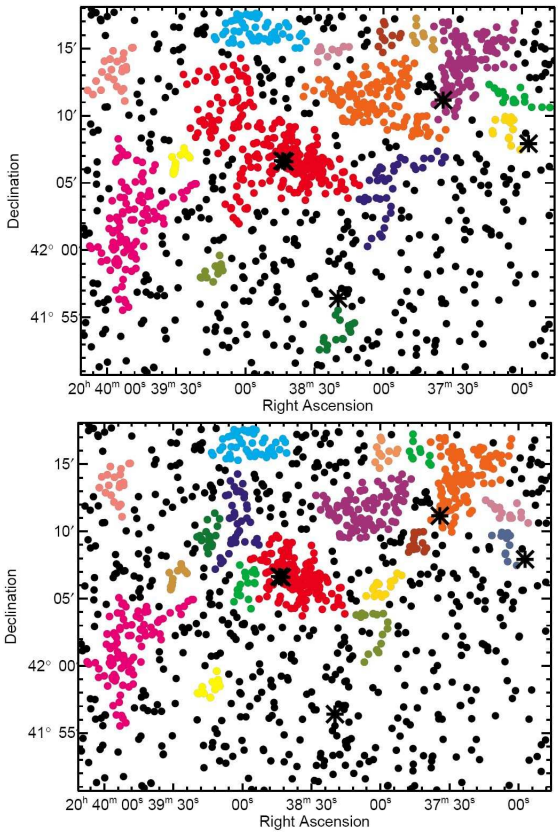

FIG. 11.— *Top*: Clusters identified using the straight-line fit method (d_c=0.43 pc) are plotted in different colors. Each color represents another cluster and the black dots represent stars that are not associated with any cluster; *Bottom*: Clusters identified using a cutoff distance of d_c = 0.40 pc are plotted in color, while sources not associated with any clusters are plotted in black. Black asterisks mark the locations of B stars found in this region.

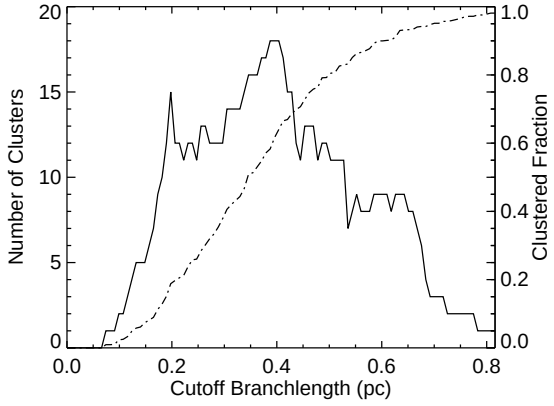

FIG. 12.— *Solid line and left y-scale*: Number of groups identified by the MST method; *Dashed line and right y-scale*: Clustered fraction of stars as a function of cutoff length.

We applied the Gutermuth et al. (2009) algorithm to identify and characterize clusters in the Diamond Ring. For each source in the region, the MST method first finds the distance to its nearest neighbor. Every source is connected by a line to another source in such a way that the total length of all the lines is minimized and there are no closed loops. The distance to its nearest neighbor

TABLE 3
DIAMOND RING CLUSTER SUMMARY[a]

Parameter	Straight-Line Fit	Ngrp Max
Number of Clusters	15	18
Percent in Clusters	67.16	58.31
Total Number in Clusters	857	744
Group Size	10-255	10-148
Cutoff Distance	0.43 pc	0.4 pc

[a] Summary of clusters identified by the cluster isolation algorithm using the straight-line fit method with a cutoff distance d_c = 0.43 pc and using d_c = 0.40 pc to maximize the number of clusters.

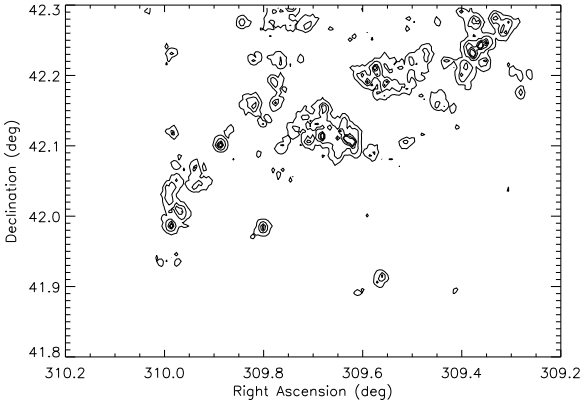

FIG. 13.— Stellar surface density contour plot for the Diamond Ring. Contours are drawn at 20, 40, 60, and 80 pc^{-2}

is called the star's branch length. Clusters are defined as a collection of stars that are connected by branches that are less than some cutoff distance and containing at least some minimum number of stars, N. We define the minimum number of stars to be N=10, attempting to minimize the identification of false groupings due to statistical fluctuations in the low density YSO distribution. To determine the cutoff distance, we plot the distribution of branch lengths in Figure 10 (right). The distribution shows two distinct regions—a short and a long branch length domain—corresponding to clustered and distributed sources respectively. While there is no definitive cutoff branch length that perfectly determines cluster membership, choosing a cutoff length that falls somewhere between these two regions is a good estimate of the divide between objects belonging to clusters and the distributed population. We fit lines through the short and long branch length parts of the distribution and extrapolate to find their intersection. The point of intersection is selected to be the cutoff length, d_c, which here equals 0.43 pc. Thus, we defined clusters in the Diamond Ring region as any group of 10 or more stars connected by lengths of no more than 0.43 pc. This cutoff distance is about half that derived by Koenig et al. (0.86 pc) for W5. This shorter cutoff length suggests that the Diamond Ring may be more densely populated with YSOs than W5.

With these criteria we identified 15 clusters, which contain 67 % of the sources. In Figure 11 (left panel), the clusters are shown in color with the distributed sources in black. B type stars are marked with black asterisks. The clusters exhibit a wide spread in size, ranging from

TABLE 4
Diamond Ring Clusters

Cluster	R.A. (J2000.0) (h m s)	Dec. (J2000.0) (° ′ ″)	N_{IR}[a]	I	II	II/I[b]	N_{emb}[c]	N_{td}[d]	Diameter (pc)
G81.51+0.43	20:38:50.06	+42:07:55.83	255	14	237	16.9(4.7)	3	1	8.1
G81.48+0.61	20:38:06.27	+42:11:48.22	133	10	122	12.2(4.0)	0	1	5.8
G81.44+0.75	20:37:26.73	+42:14:38.67	132	22	110	5.0(1.2)	0	0	4.7
G81.37+0.55	20:37:57.51	+42:05:25.25	39	4	35	8.8(4.6)	0	0	4.5
G81.71+0.34	20:39:59.88	+42:13:18.00	24	1	21	21.0(21.5)	0	2	2.4
G81.27+0.39	20:38:19.82	+41:54:25.17	17	1	16	16.0(16.5)	0	0	1.7
G81.35+0.76	20:37:05.44	+42:12:11.80	16	7	9	1.3(0.6)	0	0	2.6
G81.42+0.30	20:39:14.40	+41:58:47.48	14	3	11	3.7(2.4)	0	0	1.1
G81.56+0.35	20:39:31.17	+42:06:43.78	13	2	11	5.5(4.2)	0	0	1.0
G81.35+0.72	20:37:08.45	+42:09:48.97	13	0	13	···	0	0	1.5
G81.53+0.66	20:38:01.26	+42:16:29.25	11	1	10	10.0(10.5)	0	0	1.1
G81.54+0.61	20:38:25.87	+42:15:18.75	10	0	10	···	0	0	1.4
G81.51+0.69	20:37:46.00	+42:16:32.79	10	0	9	···	0	1	1.3

[a] Number of stars with infrared excess. Includes Class I, II, deeply embedded protostars and transition disk candidates.
[b] Number in parentheses indicates Poisson uncertainty in ratio.
[c] Number of deeply embedded protostars.
[d] Number of transition disk candidates.

10 to 255 members. Most of the larger clusters are fairly round, while some of the smaller ones are more filamentary. While most of the B type stars appear embedded inside clusters, there is one that lies just outside a smaller, more filamentary group to the South. This result is similar to what was seen in W5. While most massive stars were within large clusters, Koenig et al. found one O type star that did not lie within any cluster. However, in both W5 and the Diamond Ring, these massive stars are still found in relatively dense areas.

To investigate how our result depends on the cutoff length, we searched for the maximum number of clusters (of 10 or more stars) that could be identified by varying the cutoff length. We identified clusters for cutoff lengths from 1 to 100″, with length steps of 1″. Figure 12 shows the number of clusters and the clustered fraction as a function of cutoff distance. As d_c increases, more and more groups meet the cluster criteria. The number of clusters reaches a maximum at 18 and then begins to decline. As the cutoff length continues to increase, groups of smaller clusters get classified as one large cluster. Thus, choosing a good value for d_c relies on a compromise between including the less dense clusters and not over-simplifying substructure in the complex regions. The technique of maximizing the number of groups to determine the cutoff length was investigated in detail by Battinelli (1991).

A maximum of 18 clusters were identified for d_c = 0.40 pc. The new clusters (shown in Fig. 11, right) look similar to those for $d_c = 0.43$ pc. Two of the largest clusters were split into smaller groups, one was not found at all, and a few stars became unassociated with any cluster. An increase from 15 to 18 clusters implies that the original 0.43 pc is a reasonable cutoff distance for identifying clusters. Table 3 summarizes the cluster characteristics for each method. The fact that the overall cluster fraction appears to have changed relatively little from one value of d_c to the next provides confidence that this method is objective enough for identifying clusters in the Diamond Ring.

Table 4 lists the properties of each cluster in the Diamond Ring as derived from the straight-line fit method with $d_c = 0.43$ pc. We omit two clusters that are part of much larger clusters outside this region (the large pink cluster centered roughly at $20^h39^m45^s$, 42°02′ and the light blue cluster at 20^h9^m, 42°16′, Fig. 11, left). The clusters are named by the Galactic coordinates of the cluster centers, as determined by averaging the positions of all members. For each of the 13 listed clusters in the region, we give the number of stars with IR excess, which includes Class I and II sources and any deeply embedded protostars and transition disk sources. We list the number of each individual class and the ratio of Class II to Class I sources for each cluster. We note that small-number statistics make the ratios for the smaller clusters very uncertain: we assume Poisson uncertainty applies and list this value in Table 4 alongside each quoted ratio. The II/I ratios range from 1.3±0.6 to 21.0±21.5. The final column in the table gives the diameter of each cluster in parsecs, measured as the diameter of the smallest circle that encompasses all sources in that cluster.

We constructed a 9″ grid in the Diamond Ring region and at each point calculated the stellar surface density given by:

$$\sigma = \frac{N-1}{\pi r_N^2} \tag{2}$$

where r_N is the distance to the Nth nearest star and N=5 (Casertano & Hut 1985). The surface density contour map for the Diamond Ring is shown in Figure 13. The major groups identified in this density plot agree well with the clusters identified with the MST/cluster isolation algorithm.

3.3.2. *AFGL 2636*

The second region studied, which encompasses AFGL 2636, lies in the northeast corner of Cygnus X North. Figure 14 shows an IRAC channel 1, 2 and 4 color composite image of the region. Figure 15 displays the spatial distribution of the YSOs on a gray-scale IRAC channel 4 image. Two B stars, a B0.0±2.0 and a B5.0±3.0, sit very close together at the center of the bright molecular cloud. The B0.0 star was first classified by Gehrz et al. (1980) as a young B1-2 source. A

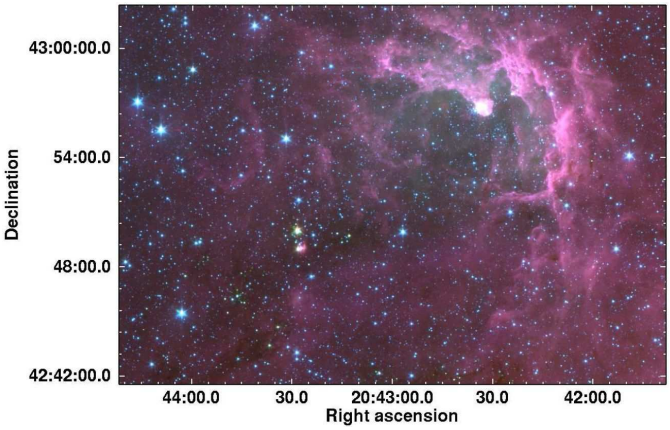

FIG. 14.— IRAC three-color composite image of AFGL 2636. *red*: 8.0 μm; *green*: 4.5 μm; *blue*: 3.6 μm.

TABLE 5
AFGL 2636 CLUSTER SUMMARY

Parameter	Straight-Line Fit	Ngrp Max
Number of Clusters	4	6
Percent in Clusters	52.90	63.29
Total Number in Clusters	235	281
Group Size	11-146	12-149
Cutoff Distance	0.38 pc	0.42 pc

dense cluster of Class II objects is distributed around the B stars and lies nestled within the bright-rimmed cloud. This cluster was first identified by Dutra & Bica (2001), who associated it with the radio H II region G82.6+0.4. A string of Class I sources lies along the rim of the cloud and extends in a wide arch to another dense group of YSOs, which reside in a dark region in the left of the image.

We performed the same clustering isolation algorithm to this region. The distribution of branch lengths in the MST is shown in Figure 15 (right panel). The straight-line fit yielded a cutoff distance of $d_c = 0.38$ pc, which led to the identification of four clusters with a clustered fraction of 52.9 percent. The clusters, which are plotted in colors in the left panel of Figure 16, range in size from 11 to 146 members. This cutoff distance is comparable to that used in the Diamond Ring region, $d_c = 0.43$ pc. The fact that the cutoff distance determined by the straight-line fit for AFGL 2636 is slightly shorter than for the Diamond Ring implies that the clusters in AFGL 2636 are denser.

As with the Diamond Ring, we varied the cutoff length in the cluster isolation algorithm from 1 to 100″ in 1″ steps. The number of clusters and the clustered fraction that resulted for each cutoff distance is plotted in Figure 17. The number of clusters vs. cutoff length plot shows two maxima at six clusters. A cutoff distance of $d_c = 0.42$ pc results in a total of 6 clusters and a larger clustered fraction of 63.3%. This cutoff distance identified the same clusters as the straight-line fit method ($d_c = 0.38$ pc), but with the addition of two new clusters. The two new clusters identified, G82.45+0.42 and G82.40+0.23, seem to exhibit definite structure, and we

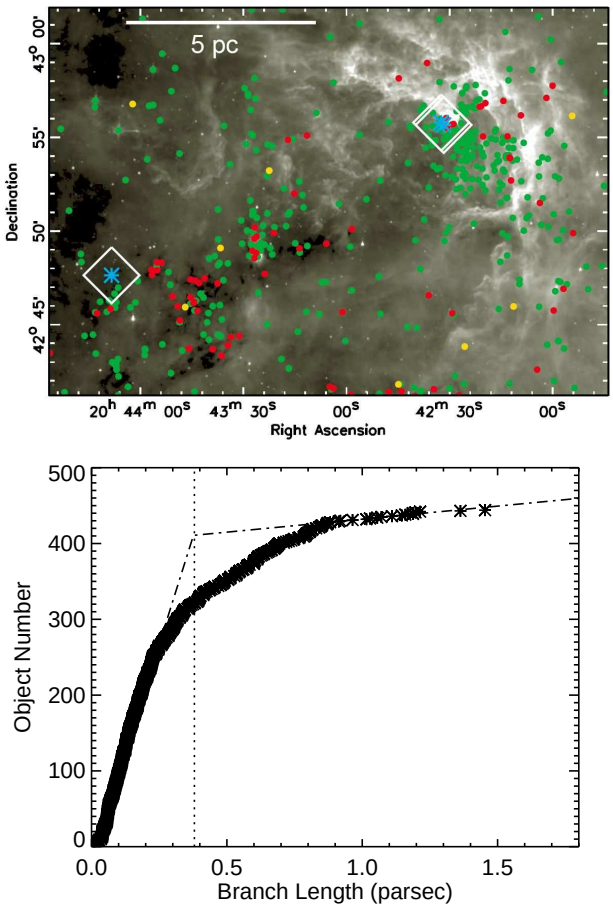

FIG. 15.— *Top*: YSO distribution overlaid on IRAC channel 4 gray-scale (8.0 μm) image of AFGL 2636. *Red*: Class0/ I; *green*: Class II; *yellow*: Transition Disks. Blue asterisks and white boxes mark B stars. *Bottom*: MST branch length distribution for AFGL 2636 region. We fit straight lines through the long and short branch length domains. The point of intersection, $d_c = 0.38$ pc, is chosen for the cutoff distance for cluster determination.

therefore chose to include them in our analysis. Table 6 lists the parameters of each of the six clusters, including the number of stars with IR excess, the number of each individual class and the ratio of Class II to Class I. The II/I ratios range from 1.6±0.5 to 12.5±3.9. The final column gives the cluster diameters in parsecs calculated in the same way as for the Diamond Ring clusters.

We constructed a 9″ grid in AFGL 2636 and at each point calculated the stellar surface density given by Equation 5. The surface density contour map for AFGL 2636 is shown in Figure 18 with contours at 20, 40, 60, and 80 pc^{-2}. The major groups identified in this density plot agree quite well with the clusters identified with the cluster isolation algorithm.

4. DISCUSSION

4.1. *Star Formation in The Diamond Ring*

Using the MST/cluster isolation method, we have identified 13 clusters in the Diamond Ring region, which are shown overlaid on an IRAC channel 4 image in Figure 19 (Left panel). To better understand the evolution of star-formation in these regions, we next need to determine the ages of each cluster. Different types of stars require different amounts of time to progress through the various

TABLE 6
AFGL 2636 Clusters

Cluster	R.A. (J2000.0) (h m s)	Decl. (J2000.0) (° ′ ″)	N_{IR}[a]	I	II	II/I[b]	N_{emb}	N_{td}	Diameter (pc)
G82.55+0.40	20:42:26.83	+42:55:33.46	149	11	137	12.5(3.9)	1	0	3.6
G82.57+0.12	20:43:44.63	+42:46:50.87	52	18	28	1.6(0.5)	4	2	3.1
G82.58+0.21	20:43:25.75	+42:50:28.60	42	6	34	5.7(2.5)	2	0	2.4
G82.61+0.06	20:44:09.14	+42:46:14.40	13	2	11	5.5(4.2)	0	0	1.1
G82.45+0.42	20:42:02.85	+42:51:17.71	13	1	12	12.0(12.5)	0	0	1.7
G82.40+0.23	20:42:37.11	+42:42:24.11	12	4	7	1.8(1.1)	0	1	2.0

[a] Number of stars with infrared excess. Includes Class I, II, deeply embedded protostars and transition disk candidates.
[b] Number in parentheses indicates Poisson uncertainty in ratio.

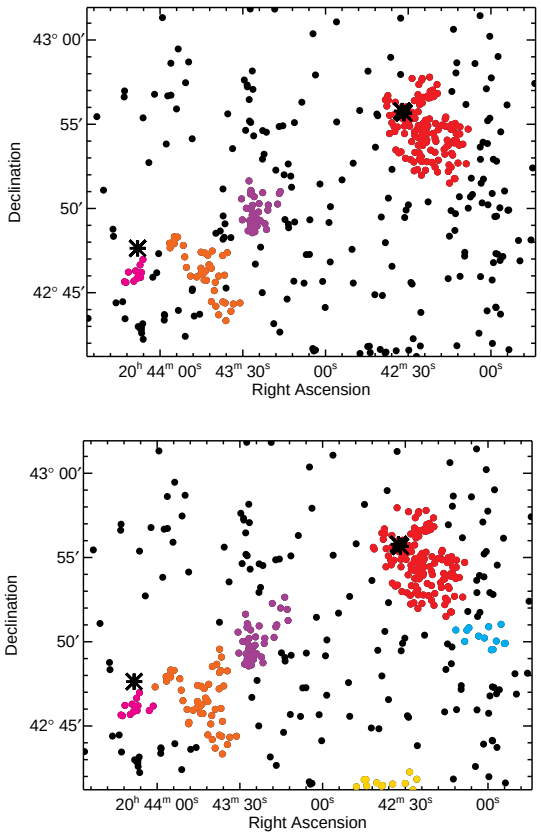

Fig. 16.— *Top*: Clusters identified using the straight-line fit method (d_c = 0.38 pc). Each color represents another cluster and the black dots represent stars that are not associated with any cluster; *Bottom*: Clusters identified using a cutoff distance of 0.42 pc are plotted in color, while sources not associated with any clusters are plotted in black.

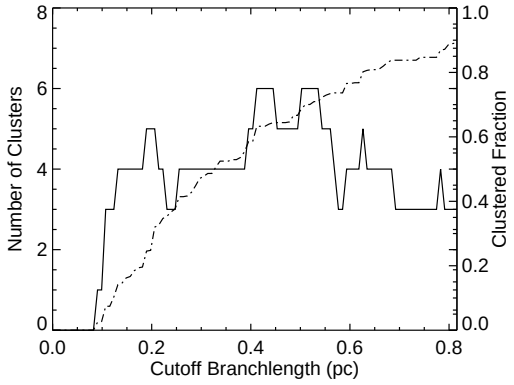

Fig. 17.— *Solid line and left y-scale*: Number of groups identified by the MST method; *Dashed line and right y-scale*: Clustered fraction of stars as a function of cutoff length.

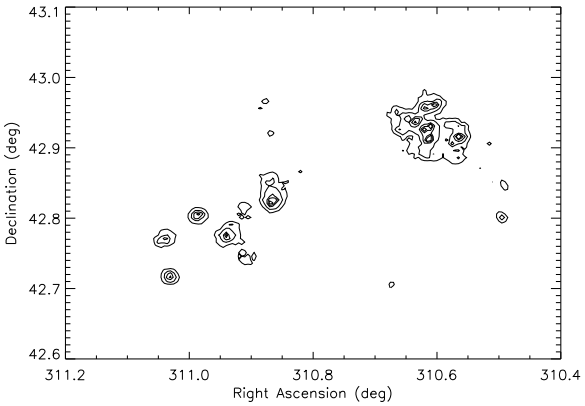

Fig. 18.— Stellar surface density contour plot of AFGL 2636. Contours are drawn at 20, 40, 60, and 80 pc^{-2}.

evolutionary stages. This variability makes determining the ages of the clusters difficult, because we cannot say that one Class I object is definitely younger than another Class II object. However, since Class I objects do represent an earlier stage of star formation than Class II, we can use the ratio of II/I sources to estimate the relative ages of the cluster. Table 4 lists the II/I ratio for each cluster in the Diamond Ring. Clusters with higher II/I ratios are dominated by Class II sources, and therefore should be relatively older.

According to the II/I ratios, the red cluster, G81.51+0.43, appears to be the oldest with a II/I ratio of 16.9±4.7 (G81.71+0.34 has a higher ratio but with much larger uncertainty). This cluster, which sits at the tip of the Diamond Ring and contains three B stars, is dominated by Class II sources and perhaps represents the earliest phase of star formation in the Diamond Ring region. One of the oldest clusters, G81.48+0.61 (orange), lies at the center of the Diamond Ring. With a II/I ratio of 12.2±4.0, it may have formed slightly after the red cluster. We have the optical spectrum from only one star in this orange cluster, which was found to be an F type star.

Most of the other clusters that surround the red and orange clusters have lower II/I ratios. G81.44+0.75 (purple) contains 22 class I sources, which is the most of

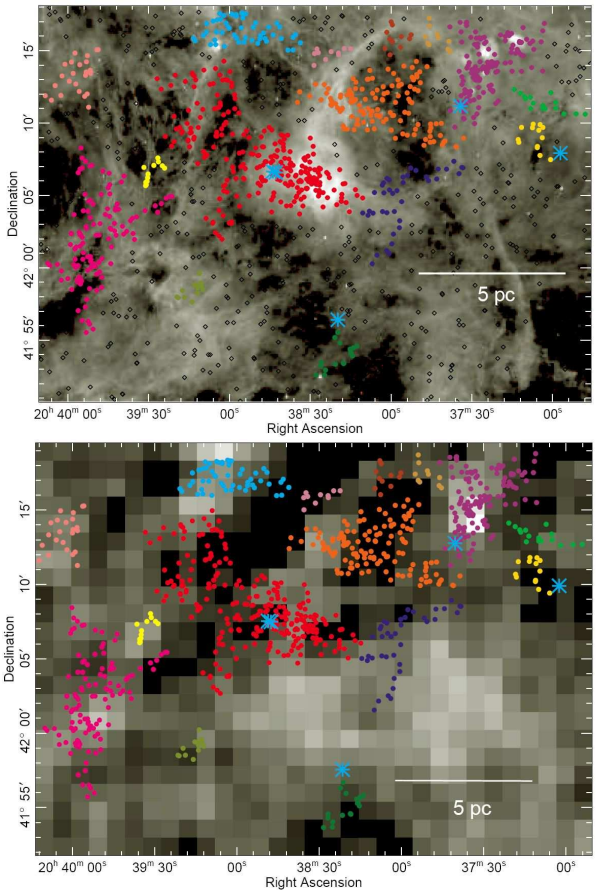

FIG. 19.— *Top*: The clusters identified in the Diamond Ring region using d_c = 0.43 pc overlaid on an IRAC channel 4 gray-scale image. *Bottom*: A_V extinction map of the Diamond Ring generated with 2MASS photometry with clusters overlaid. White indicates higher extinction. Blue asterisks mark B stars.

all the clusters in the Diamond Ring. It has a II/I ratio of 5.0±1.2, implying that it is younger than the red and orange. Other younger clusters include G81.35+0.76 (green, top right), G81.42+0.30 (olive, bottom left), G81.56+0.35 (yellow, left) and G81.37+0.55 (blue) with II/I ratios of 1.3±0.6, 3.7±2.4, 5.5±4.2, and 8.8±4.6, respectively. These clusters lie in a ring around the older red and orange clusters.

The distribution of these clusters helps us to understand the star formation history of the Diamond Ring. It appears that the initial star formation occurred in the red and orange clusters. Then winds and radiation from the most massive stars in the red cluster sent shocks through the dust and gas in the surrounding regions, possibly inducing the subsequent generation of star formation, represented by the smaller, younger surrounding clusters. This situation is similar to what was found in W5 and NGC 602 (Koenig et al. 2008; Carlson et al. 2007). Figure 19 (right panel) shows the clusters plotted on the visual extinction map of this region, where white indicates higher extinction. The red and orange clusters lie in very dark regions, implying little extinction. The young clusters (purple, green, blue, olive, yellow), on the contrary, tend to lie in areas of higher extinction. These young clusters still reside within their dusty natal molecular clouds. However, in the older red and orange clusters, winds and radiation from the massive stars have effectively removed the dust and gas from their parental molecular clouds. Although we did not find any O type stars in our spectral survey, several objects coincident with the red and orange clusters have $r'i'H\alpha$ photometry consistent with a spectral type earlier than B0 at the distance and extinction of Cygnus X. The fact that the red and orange clusters have had time to blow away their molecular clouds while the others have not is consistent with our picture of star formation in the Diamond Ring.

4.2. *Star Formation in AFGL 2636*

AFGL 2636 lies on the outskirts of Cygnus X North and exhibits similar structure to the Diamond Ring. The clusters are displayed on an IRAC channel 4 image in Figure 20. The largest and densest cluster is G82.55+0.40 (red), which contains two B type stars. As with the Diamond Ring region, we found 3 objects coincident with the red cluster, whose optical photometry is consistent with a spectral type earlier than B0 at the distance and reddening of Cygnus X. This cluster has a Class II/I ratio of 12.5±3.9 which suggests that it represents the oldest phase of star formation in this region. The cyan cluster G82.40+0.23 which sits just below the red also has a high II/I ratio of 12.0±12.5, but this large range makes its evolutionary status uncertain. The other clusters have significantly lower II/I ratios. The next largest cluster, G82.57+0.12 (orange) contains 18 Class I sources and has a II/I ratio of 1.6±0.5, making it likely a much younger cluster. The nearby pink and purple clusters, G82.61+0.06 and G82.58+0.21, are also relatively young, with II/I ratios of 5.5±4.2 and 5.7±2.5, respectively. The gold cluster, G82.40+0.23, contains 4 Class I sources and 7 Class II sources. It is part of the long chain of Class I stars that forms a wide circle around this region. The relative ages of the clusters suggest that these latter objects are a later generation of star formation, which is also consistent with their association with infrared dark clouds (IRDCs) to the southeast of the AFGL 2636 cavity.

In the right panel of Figure 20, the clusters are shown overlaid on the visual extinction map for this region. In contrast to the Diamond Ring, all six clusters lie within areas of higher extinction. However, we can see that the orange, purple, pink and gold clusters reside in regions of higher extinction than the red and cyan clusters. This trend is consistent with our conclusion that the red and cyan clusters are the oldest in the region. The younger clusters are still deeply embedded in molecular clouds, while the red and cyan clusters have had time to remove some of their surrounding dust and gas.

In AFGL 2636, there are 52 Class I stars and 214 Class II stars in clusters, whereas, in the Diamond Ring, there are 65 Class I sources and 618 Class II sources in clusters. Thus, the II/I ratio for all the clusters in the Diamond Ring (9.5±1.2) is about twice that for AFGL 2636 (4.1±0.64). We therefore conclude that AFGL 2636 is likely to be younger than the Diamond Ring, which lies in the center of Cygnus X North.

4.3. *Clustered Fractions*

We sought to find what fraction of young stars form in clusters as opposed to in distributed populations. However, since defining cluster membership is somewhat arbitrary, this question is difficult to answer. Using the

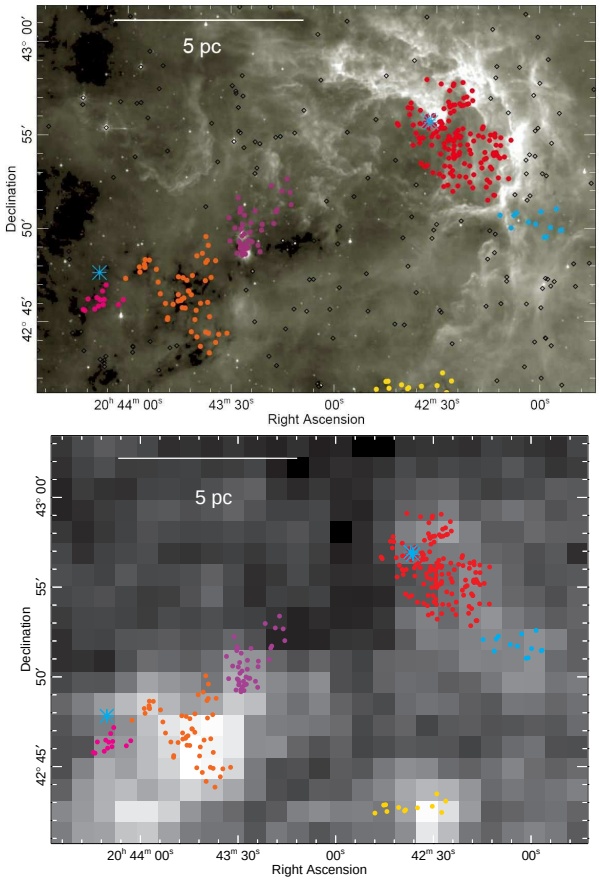

FIG. 20.— *Top*: Clusters identified using $d_c = 0.42$ pc overlaid on IRAC channel 4 gray-scale image of AFGL 2636; *Bottom*: A_V extinction map generated with 2MASS photometry with clusters overlaid. In both plots, B stars are marked with blue asterisks.

straight-line fit method with the cluster isolation algorithm, we found that 67% of YSOs in the Diamond Ring region and 53% of YSOs in AFGL 2636 belong to clusters of at least 10 members. However, using a cutoff distance that maximizes the number of clusters, we found that 58% and 63% of YSOs are in clusters in the Diamond Ring and II, respectively. Carpenter (2000) found that ∼75% of low mass stars form in clusters. Thus the regions in Cygnus X, with clustered fractions of 53–67% fall slightly below this level. This result may be more comparable to the work of Koenig et al. (2008) who found that between 44 and 70% of YSOs in W5 reside in clusters with ≥10 members (depending on the choice of clustering cutoff length). However, it should be noted that the study of W5 covered a larger area than our smaller regions of Cygnus X, and therefore included more distributed sources. The Diamond Ring region and AFGL 2636 were chosen because they contain particularly dense clusters around massive stars. If we looked at the entire Cygnus X North region, the clustered fraction would likely be lower than 53–67%.

5. CONCLUSIONS AND FUTURE WORK

We have used optical spectroscopy from FAST and Hectospec to classify possible OB sources in Cygnus X North. We classified a total of 536 sources and found a total of 24 B type stars and no O type stars, although several candidate O stars are evident in the IPHAS survey's photometric catalog. To verify that the spectrally observed stars are indeed members of the Cygnus X complex, we plotted these sources on an H-R diagram. We found that most of the stars seemed to fall on a line consistent with a distance of 1.7 kpc, confirming their association with Cygnus X.

We used *Spitzer* IRAC and MIPS photometry to identify and classify YSOs in Cygnus X North. We found 670 Class I, 7,249 Class II, 112 transition disk, and 200 embedded protostellar sources. We identified two regions in Cygnus X North that contained a dense grouping of YSOs around massive B stars. We used a minimal spanning tree and cluster isolation technique to study the spatial distribution of YSOs in these two regions. We found that 58–67% of YSOs belong to clusters of ≥10 members in the Diamond Ring region and 53–63% of YSOs belong to clusters of ≥10 members in AFGL 2636.

We used the ratio of Class II/I sources in each cluster to approximate a formation history of the clusters in each region assuming that a higher ratio of Class II to Class I objects indicates a more evolved (and thus older) cluster. We found that in both regions, a dense cluster around one or more massive stars seems to have formed first. A number of younger clusters are found surrounding the older cluster. These younger clusters may have formed when stellar winds and radiation from the most massive stars in the central cluster triggered a new generation of star formation.

There remains much to be understood about the history of star formation in the Cygnus X complex. By applying new algorithms for defining cluster memberships, we can hope to better characterize the structure of clusters in Cygnus X. As was mentioned earlier in this paper, our FAST survey may have missed some of the brightest sources in Cygnus X. Future studies will seek to locate and classify the most massive stars in the region that were missed by our survey and will allow us to better understand the evolution of star formation across the entire Cygnus X region.

This work is based on observations made with the *Spitzer Space Telescope*, which is operated by the Jet Propulsion Laboratory, California Institute of Technology, under contract with NASA. This work was supported in part by the National Science Foundation Research Experiences for Undergraduates (REU) and Department of Defense Awards to Stimulate and Support Undergraduate Research Experiences (ASSURE) programs under Grant no. 0754568 and by the Smithsonian Institution.

Facilities: MMT(Hectospec), FLWO(FAST), 2MASS (JHK_S), Spitzer (IRAC, MIPS)

REFERENCES

Allen, L. E. et al. 2007, Protostars and Planets V, eds. B. Reipurth, D. Jewitt, & K. Keil (Univ. Arizona Press), 361

Battinelli, P. 1991, A&A, 244, 69

Carey, S. J., et al. 2009, PASP, 121, 76
Carlson, L. R., et al. 2007, ApJ, 665, 109
Carpenter, J. M. 2000, AJ, 120, 3139
Cartwright, A., & Whitworth, A. P. 2004, MNRAS, 348, 589
Casertano, S., & Hut, P. 1985, ApJ, 298, 80
Castor, J., McCray, R., & Weaver, R. 1975, ApJ, 200, L107
Comerón, F., Pasquali, A., Figueras, F., & Torra, J. 2008, A&A, 486, 453
Currie, T., et al. 2010, arXiv:1002.1715
Downes, D., & Rinehart, R. 1966, ApJ, 144, 937
Drew, J., et al. 2005, MNRAS, 362, 753
Dutra, C. M., & Bica, E. 2001, A&A, 376, 434
Elmegreen, B. G., & Lada, C. J. 1977, ApJ, 214, 725
Fabricant, D., Hertz, E., & Szentgyorgyi, A. H. 1994, Proc. SPIE, 2198, 251
Fabricant, D. et al. 1998, PASP, 110, 79
Fazio, G. G. et al. 2004, ApJ, 154, 10
Flaherty, K. M., Pipher, J. L., Megeath, S. T., Winston, E. M., Gutermuth, R. A., Muzerolle, J., Allen, L. E., & Fazio, G. G. 2007, ApJ, 663, 1069
Gehrz, R. D., et al. 1980, ApJ, 85, 1071
González-Solares, E. A. et al. 2008, MNRAS, 388, 89
Gutermuth, R. A. et al., 2008, ApJ, 674, 336
Gutermuth, R. A., Megeath, S. T., Myers, P. C., Allen, L. E., Pipher, J. L., & Fazio, G. G. 2009, ApJS, 184, 18
Hernández, J., Calvet, N., Briceño, C., Hartmann, L., Berlind, P. 2004, ApJ, 127, 1682
Hernández, J. 2005, Ph.D. dissertation, Universidad de Los Andes, Merida, Venezuela
Hernández, J., Hartmann, L., Calvet, N., Jeffries, R. D., Gutermuth, R., Muzerolle, J., & Stauffer, J. 2008, ApJ, 686, 1195
Hora, J. L., et al. 2010, in prep
Jordi, K., Grebel, E. K., & Ammon, K. 2006, A&A, 460, 339
Kenyon, S. J., & Hartmann, L. 1995, ApJS, 101, 117
Koenig, X. P., et al. 2008, ApJ, 688, 1142
Knödlseder, J. 2000, A&A, 360, 539
Lada, C. J. 1991, in The Physics of Star Formation and Early Stellar Evolution, ed. C. J. Lada & N. D. Kylafis (Dordrecht: Kluwer), 329
Lada, C. J., & Lada, E. A. 2003, ARA&A, 41, 57
Lawrence, A., et al. 2007, MNRAS, 379, 1599
Le Duigou, J.-M., & Knödlseder, J. 2002, A&A, 392, 869
Lockman, F. J. 1989, ApJS, 71, 469
Lucas, P. W., et al. 2008, MNRAS, 391, 136
Marston, A. P. 2004, ApJS, 154, 333
Mizuno, D. R., et al. 2008, PASP, 120, 1028
Piddington, J. H., Minnett, H. C., 1952, Aust. J. Sci. Res. A Phys. Sci., 5, 17
Povich, M. S., et al. 2009, ApJ, 696, 1278
Povich, M. S., & Whitney, B. A. 2010, ApJ, 714, L285
Reipurth, B., & Schneider, N. 2008, in ASP, Handbook of Star Forming Regions, Vol. 1, ed. B. Reipurth (San Francisco, CA: ASP), 36
Rieke, G. H. et al. 2004, ApJ, 154, 25
Robitaille, T. P. et al. 2008, AJ, 136, 2413
Ruch, G. T., Jones, T. J., Woodward, C. E., Polomski, E. F., Gehrz, R. D., & Megeath, S. T. 2007, ApJ, 654, 338
Schlegel, D. J., Finkbeiner, D. P., & Davis, M. 1998, ApJ, 500, 525
Schneider, N., Bontemps, S., Simon, R., Jakob, H., Motte, F., Miller, M., Kramer, C., & Stutzki, J. 2006, A&A, 458, 855
Schneider, N., Simon, R., Bontemps, S., Comerón, F., & Motte, F. 2007, A&A, 474, 873
Siess, L., Dufour, E., & Forestini, M. 2000, A&A, 358, 593
Skrutskie, M. F., et al. 2006, AJ, 131, 1163
Strömgren, B. 1939, ApJ, 89, 526
Tokarz, S. P., & Roll, J. 1997, in ASP Conf. Ser. 125, Astronomical Data and Software Systems VI, ed. G. Hunt & H. E. Payne (San Francisco:ASP), 140
Wendker, H. J. 1984, A&AS, 58, 291
Wendker, H. J., Higgs, L. A., & Landecker, T. L. 1991, A&A, 241, 551
Werner, M. W. et al. 2004, ApJ, 154, 1
Zinnecker, H., & Yorke, H. W. 2007, ARA&A, 45, 481

TABLE 7
Optical Spectroscopy Classifications

Source	r' (mag)	r' error (mag)	i' (mag)	i' error (mag)	Sp. Type	Type Err.	A_V (mag)
J203534.33+414946.7	12.368	0.001	12.001	0.001	G1.0	2.0	1.2
J203535.86+414925.7	12.447	0.001	11.999	0.001	G4.0	2.0	1.6
J203538.92+415641.7	12.410	0.001	12.091	0.001	F8.0	2.0	1.1
J203548.37+420536.0	12.603	0.001	12.217	0.001	F9.0	2.0	1.3
J203556.64+414529.1	13.165	0.001	12.585	0.001	F8.5	2.0	2.3
J203614.10+422924.0	17.018	0.004	15.379	0.005	K1.0	1.0	7.1
J203615.46+420409.8	16.539	0.007	15.732	0.007	K5.5	1.0	1.8
J203626.20+414624.0	11.682	0.001	11.269	0.001	F7.5	2.0	1.6
J203626.62+423852.1	12.934	0.001	12.228	0.001	B3.0	2.0	5.1
J203629.11+420826.1	12.320	0.001	11.970	0.001	F9.5	2.0	1.1

Note. — This Table is published in its entirety in the electronic edition of the *Astrophysical Journal*. A portion is shown here for guidance regarding its form and content. The 'Source' column gives the object name, which contains its Right ascension and Declination coordinates J2000.0.

APPENDIX

SPECTRAL SAMPLE

Table 7 lists the spectral classifications of the sources for which we obtained FAST spectra. The source names were derived from the position using the minutes and seconds of right ascension and degrees and minutes of declination. The sources are listed with their spectral types and errors, which were determined by SPTclass.